

FULL PAPER

Open Access



Insight into the 2017 Mainling M_w 6.5 earthquake: a complicated thrust event beneath the Namche Barwa syntaxis

Wei Xiong¹, Wei Chen¹, Yangmao Wen², Gang Liu¹, Zhaosheng Nie^{1*}, Xuejun Qiao¹ and Caijun Xu²

Abstract

On November 18, 2017, the Mainling M_w 6.5 earthquake occurred on the northern Namche Barwa syntaxis and was the largest earthquake in the syntaxis and surrounding areas since the Zayu M_w 8.4 earthquake in 1950. Due to inconvenient access and the severe environment in the Namche Barwa syntaxis area, the motions and tectonic structures of most faults remain unclear. Sparsely distributed seismic observation stations make the seismogenic fault and focal mechanism of the Mainling earthquake controversial. We adopt interferometric synthetic aperture radar (InSAR) to invert the slip distribution of this event by defining the fault geometry with relocated aftershocks. Our preferred model suggests that the 2017 Mainling earthquake ruptured two blind faults beneath the Namche Barwa syntaxis. The ruptures were dominated by thrusts with slight right-lateral strike-slip components. The slips on the two faults are equivalent to moment magnitudes of M_w 6.12 and M_w 6.34, with maximum dislocation magnitudes of 0.36 m and 0.43 m, respectively. The model fits well with the InSAR observations and the distribution of aftershocks. The results from the Coulomb stress simulation indicate that the stress loading caused by strong historical events promoted the occurrence of the 2017 Mainling earthquake. Compared with the seismogenic faults of the Mainling earthquake, the larger thrust faults in the southern Namche Barwa syntaxis can generate larger earthquakes. Therefore, we assume that $M_w > 6.5$ earthquakes may occur beneath the Namche Barwa syntaxis and that the seismic risk has been further promoted by historical events.

Keywords: 2017 Mainling earthquake, InSAR, Slip distribution, Coulomb stress change, Seismic risk

Introduction

In the Himalayan region, the Indian Plate is sliding beneath the Eurasian Plate at a rate of 40–50 mm/a, making the 2500-km-long Himalayan arc the most spectacular topographic manifestation on Earth in ~ 50 Ma (Yin and Harrison 2000). The Himalayan collision zone is delimited along the EW direction by the syntaxes Namche Barwa in the east (96°E) and Nanga Parbat in the west (74°E) (Burg et al. 1998; Zeitler et al. 2014). In contrast to the N–S thrust-dominated slip in the Himalayan thrust zone, the tectonic movement in the Namche Barwa syntaxis has developed not only an imbricate subduction

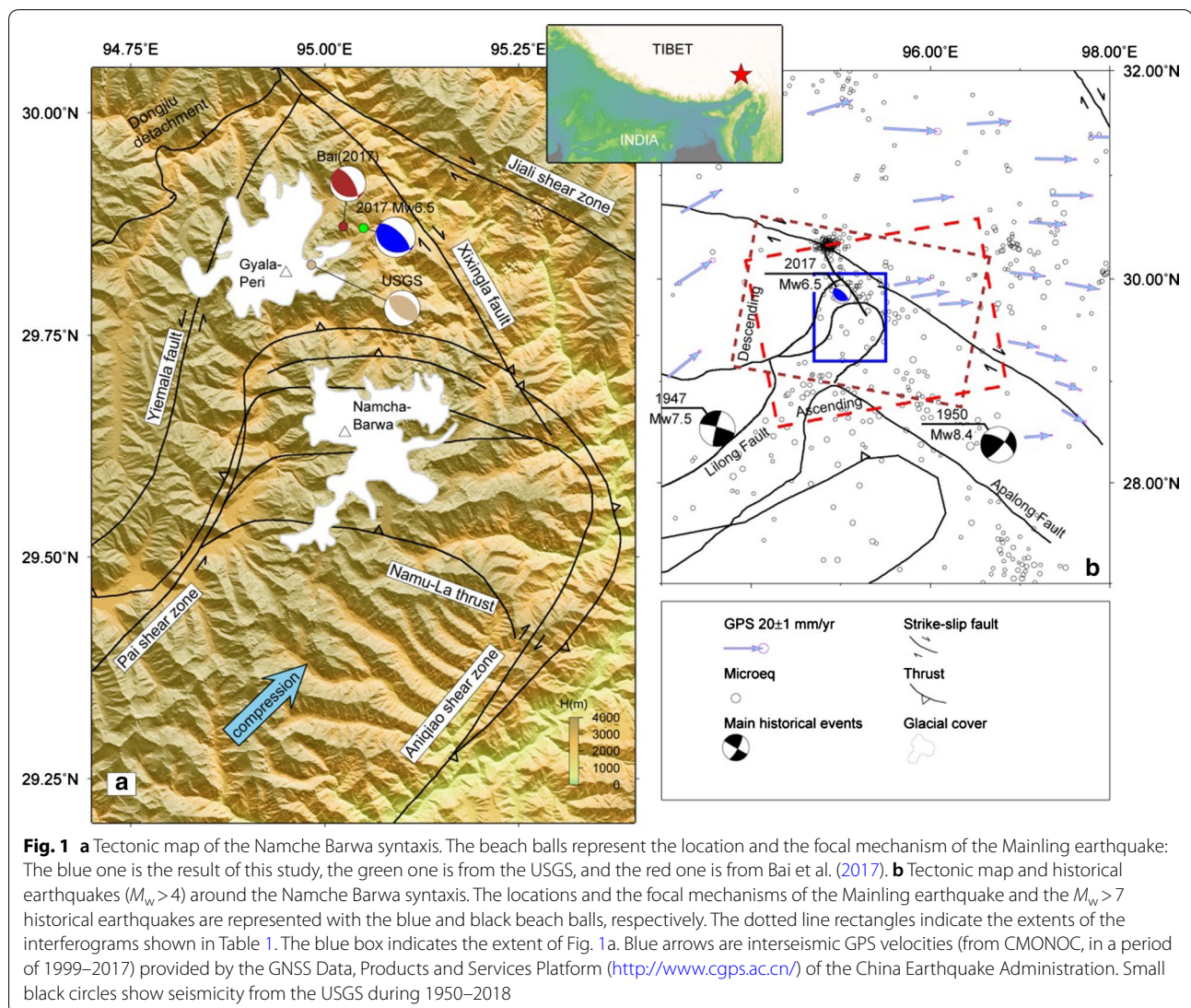
structure beneath the Namche Barwa Mountains but also strong strike-slip activity around its periphery (Tapponnier et al. 2001; Ding et al. 2001; Yang et al. 2018a; Fig. 1). As a part of the eastern boundary of the Namche Barwa syntaxis, the Xixingla fault is located on the northeastern side of the syntaxis. It is a dextral strike-slip fault with thrust components where small and moderate earthquakes occur frequently, which makes it one of the most active faults in the Namche Barwa syntaxis (Ding et al. 2005; Bai et al. 2017).

The geological environment in the Namche Barwa syntaxis is complex. Both Mount Gyala Peri (approximately 7294 m above sea level) and Mount Namche Barwa (approximately 7782 m above sea level) are located here, accompanied by glacier development (Fig. 1). Due to severe natural conditions and scarce geological and geodetic data, the movement features

*Correspondence: niezhaosheng@126.com

¹ Key Laboratory of Earthquake Geodesy, Institute of Seismology, CEA, Wuhan 430071, China

Full list of author information is available at the end of the article



and tectonic structures of most faults in this area are not clear. On November 18, 2017, the Mainling M_w 6.5 earthquake occurred on the northern Namche Barwa syntaxis. The epicenter was located on the southwest side of the Xixingla fault, and the focal mechanism was dominated by thrusts (according to the Global Centroid Moment Tensor (GCMT), last accessed December 1, 2017, Table 2). The Mainling earthquake is the largest earthquake to occur in the Namche Barwa syntaxis and surrounding areas since the Zayu M_w 8.4 earthquake in 1950 (Hu and Yao 2018; Yu et al. 2018). Hence, studying the focal mechanism and slip distribution of this earthquake is of great significance for determining the seismogenic fault and understanding the dynamic mechanism of the eastern Himalayan orogenic belt.

However, the focal mechanism of the Mainling earthquake is currently controversial. Bai et al. (2017) recalculated the location and origin time of the Mainling earthquake based on waveforms and arrival times recorded by local and teleseismic networks. The earthquake was considered as a north-dipping thrust event in the Xixingla fault zone. Recent seismic relocation studies have shown similar results that the earthquake occurred on a steep north-dipping fault plane (Wei et al. 2018; Yin et al. 2018a). Teleseismic data provide an approximate epicenter location for this event, but they are not sufficient to resolve the detailed subsurface structure. Spaceborne interferometric synthetic aperture radar (InSAR) observations with high spatial coverage afford a good opportunity to determine the source characteristics,

but the results are surprisingly different: Yu et al. (2018) inverted the slip distribution of the Mainling earthquake as constrained by Sentinel-1 radar interferometry and concluded that the earthquake occurred on a south-dipping blind reverse fault with an obvious right-lateral component, while Li et al. (2018) considered the earthquake a thrust and left-lateral event based on the same InSAR data (Table 2). The key to determining the seismogenic fault is to identify the nodal plane of the Mainling earthquake, and a combined inversion with both InSAR and aftershock relocation data may provide more information.

In addition, 27 $M_w > 6.0$ earthquakes have occurred in the Namche Barwa syntaxis area since 1900. Two of them are $M_w > 7.0$ earthquakes: the Zayu M_w 8.4 earthquake in 1950 and the Lang M_w 7.5 earthquake in 1947. Whether the occurrence of the Mainling earthquake is related to the above-mentioned historical events and what the trend is of the seismic activities on the Namche Barwa syntaxis urgently need to be studied.

In this paper, we use Sentinel-1 radar interferometry data to determine the coseismic deformation of the 2017 Mainling earthquake and to further invert the slip distribution. In the inversion, we use the aftershock relocation data (Yin et al. 2018b) to constrain the seismogenic fault geometry. Based on a viscoelastic layered crust model, we then study the stress disturbance prior to the 2017 Mainling earthquake caused by two historical strong earthquakes in the neighboring area of the Namche Barwa syntaxis and analyze the correlation between the historical events and the Mainling earthquake. Finally, we analyze the seismic risk in the Namche Barwa syntaxis, considering the influence of the Coulomb stress change induced by the Mainling earthquake.

InSAR data processing and fault slip modeling

InSAR data processing

We analyzed both ascending and descending InSAR data covering the Mainling region as imaged by the Sentinel-1 satellite of the European Space Agency (ESA) in image wide mode (Fig. 1b; Table 1). The data use terrain observation with progressive scan synthetic aperture radar (TOPS SAR) technology to enhance radiation performance by effectively reducing the scalloping effect, which

occurs during wide-field imaging. The pairs of Sentinel-1A images have the shortest temporal interval of 12 days to minimize the effect of post-seismic deformation. In addition, the data have short perpendicular baselines of 32.9 m and 9.6 m to reduce the impact of the digital elevation model (DEM) error (Simons et al. 2002) and the possibility of spatial decorrelation.

The GAMMA software is used to produce the Sentinel-1 interferograms. A ratio of 10:2 for range and azimuth original data is multi-looked to improve the signal-to-noise ratio. The topographic effect is removed using the 90-m resolution Shuttle Radar Topography Mission (SRTM) DEM. We use the self-adaptive filtering method to reduce phase noise in differential interferograms, and then, the statistical-cost network-flow algorithm (SNAPHU) is used to perform phase unwrapping (Chen and Zebker 2000). Finally, after geocoding, we obtain the coseismic deformation field of the Mainling earthquake in the line of sight (LOS) direction (Fig. 2). On the southwest side of the coseismic deformation field, a “bull’s-eye” pattern of negative LOS deformation is discernable (Additional file 1: Figure S1), with a maximum LOS displacement of -0.164 m. While on the northeast side, a positive LOS deformation area is detected, although the displacements are relatively low (Fig. 2). The asymmetrical coseismic deformation pattern is consistent with a focal mechanism dominated by thrust slip, perhaps with some lateral slip (He et al. 2018). These characteristics are similar to those of previous studies (Yu et al. 2018; Li et al. 2018). We adopt the 1D covariance function (Parsons et al. 2006) to estimate the uncertainty of the LOS displacements. The standard deviations are smaller than 0.014 m (Table 1).

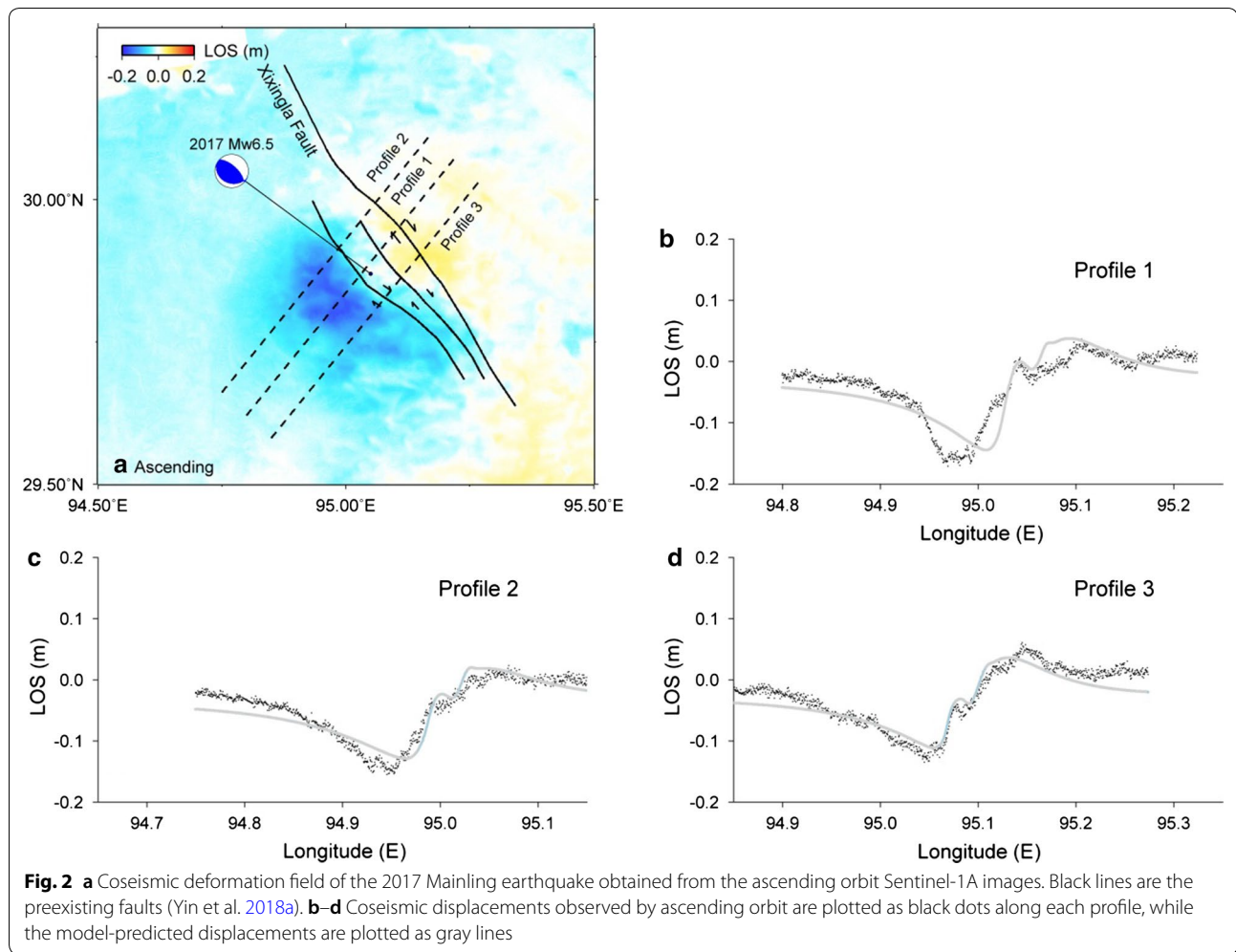
Note that the quality of the ascending InSAR data is significantly better than that of the descending data. In the interferogram derived from the ascending data, there are obvious fringes, and the deformations are concentrated at the epicenter. However, in the interferogram derived from the Sentinel-1A descending images, the coseismic signals are difficult to identify and show no continuous fringes (Additional file 1: Figure S1). The same phenomenon exists in Yu et al. (2018), and their inversion results are also poorly fitted to the descending data. Li et al. (2018) did not adopt descending data

Table 1 The details of the Sentinel-1 images used in this study

Flight direction	Image mode	Master YYYYMMDD	Slave YYYYMMDD	Time interval (d)	Perpendicular baseline (m)	σ (m)	α (km)
Descending	IW	20171106	20171118	12	9.6	0.0134	5.6661
Ascending	IW	20171111	20171123	12	32.9	0.0124	2.5166

σ : Standard deviations are calculated with all points in the undeformed area

α : The e-folding correlation length scale of the 1D covariance function



for inversion. Considering that we can use the aftershock relocation data to constrain the seismogenic fault geometry, we do not use the descending data in the inversion.

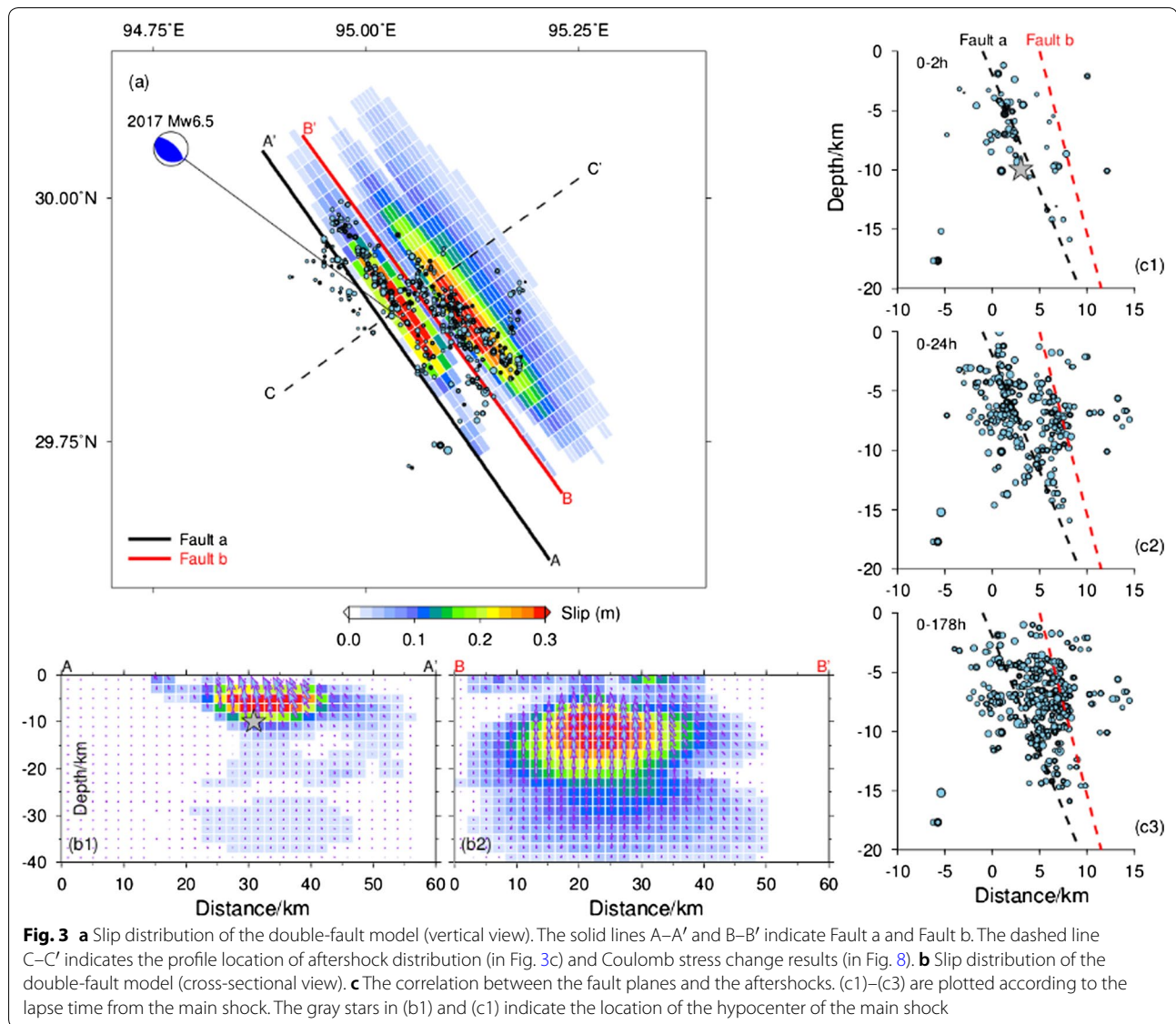
Aftershocks

With the waveform data recorded by the Nyingchi array, Yin et al. (2018a) analyzed the spatiotemporal evolution of early aftershocks following the Mainling earthquake. More than 312 $M_w > 0.3$ aftershocks between November 18, 2017, and November 25, 2017, were obtained (Fig. 3), and the 1-sigma errors of the aftershocks are approximately 0.555, 0.621 and 0.992 km in the east, north and up directions, respectively. The aftershock distribution along the C–C' sections in Fig. 3a, c shows that the earthquake occurred on a steep north-dipping plane, while the horizontal distribution map shows that the aftershocks mainly occurred on at least two small-scale faults. The aftershock distribution characteristics are similar to those in Wei et al. (2018). The data suggest that the Mainling earthquake ruptured two nearly parallel faults

instead of only one fault. In addition, at least two events could be found in the source time function (Li et al. 2018) of the Mainling earthquake, which is consistent with the double-fault hypothesis. We build the single-fault model and the double-fault model separately in the inversion and discuss the reliability of the models.

Finite-fault modeling

The quad-tree sampling method is used to downsample the coseismic deformation field from InSAR, which can both reduce the amount of data and preserve deformation data to a large extent (Jonsson et al. 2002). The noise area is masked to avoid sampling points gathered locally or at the edge. Simultaneously, we set the maximum and minimum windows for sampling and uniformly sample in the areas that are not within this range to make the distribution of sampling results more reasonable, that is, to avoid too few sampling points in the far field or too many in the near field. The maximum and minimum sampling windows are 256 (approximately 12 km × 12 km) and 16



(approximately $0.8 \text{ km} \times 0.8 \text{ km}$), respectively. The deformation gradient threshold is set to 2 cm. The total number of InSAR points ultimately involved in the inversion is 1063 (ascending orbit) after downsampling, which can well retain the major features of the original interferograms (Additional file 1: Figure S1).

Since the distribution of aftershocks is north-dipping, we select the parameters strike = 328° and dip = 66° according to the GCMT as the initial fault parameters. A rectangular fault plane covering an area of $60 \text{ km} \times 40 \text{ km}$ is built in a homogeneous elastic and isotropic half-space (Okada 1992) (with $V_s = 3.52 \text{ km/s}$; $V_p = 6.0 \text{ km/s}$; $\rho = 2720 \text{ kg/m}^3$, as shown in Table 3) for the single-fault model, while two fault planes with scales of $60 \text{ km} \times 40 \text{ km}$ and $50 \text{ km} \times 40 \text{ km}$ are built for

the double-fault model. The top boundaries of the fault planes are on the ground surface. The fault traces of double-fault model are selected based on the two preexisting faults (Fig. 2a), while the trace of single-fault model is selected on the fault on the west side. The traces are fixed in the inversion. The fault planes are divided into subfaults with a size of $2 \text{ km} \times 2 \text{ km}$.

We determine the single-fault model's trace is on the west side according to the following reasons: (a) The epicenter of the earthquake (Bai et al. 2017) is located between the two preexisting faults (Fig. 3). If the single-fault model's trace is on the west side, the fault plane should be east-dipping. And if the single-fault model's trace is on the east side, the fault should be west-dipping. The results of the aftershock (Yin et al.

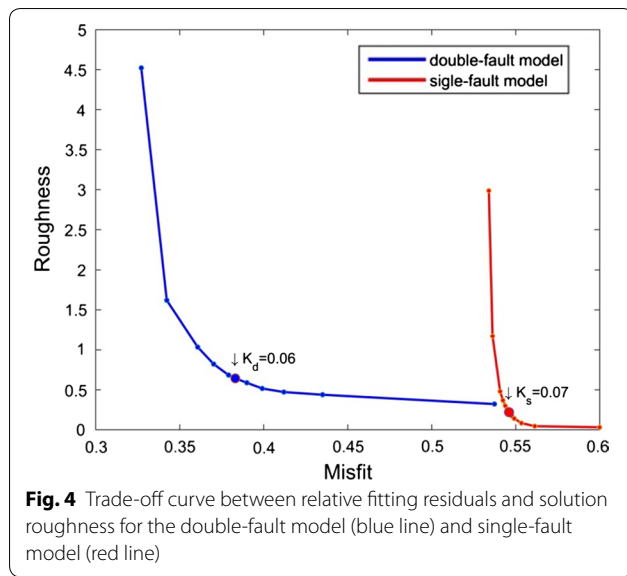


Fig. 4 Trade-off curve between relative fitting residuals and solution roughness for the double-fault model (blue line) and single-fault model (red line)

2018a; Wei et al. 2018) show that the Mainling earthquake should be east-dipping. (b) The time series of the aftershocks indicate that the rupture of the Mainling earthquake began on the fault on the west side.

Based on a variable-slip rupture model, we apply the least squares algorithm and the constraint steepest descent method (Wang, 2010) that allows variable rake to invert for the slip of each subfault. We set the rake to range from 80° to 120° . Coseismic slip distributions are inverted with a Laplacian operator to ensure reasonable solutions. The Laplacian smoothing factors are selected according to trade-off curves between weighted misfit and solution roughness for both single-fault model and double-fault model (Fig. 4). The strike angle is fixed at 328° in the inversion. However, we do not fix the dip angles as previous studies have done (e.g., Li et al. 2018), but we use a grid search to determine the optimum values in a range of $\pm 20^\circ$ with an interval of 1° to best fit the InSAR data. The results for the fault parameters are shown in Table 2. After nearly 2000 regression analyses to optimize the model, we obtain the fault slip distribution (Fig. 3a, b), simulated coseismic deformation field (Fig. 5c, d) and inversion residual (Fig. 5e, f).

Both single-fault and double-fault models present a thrust-dominated mechanism, with maximum slips of 0.34 m and 0.35 m, respectively. The mean residual of the single-fault model is 0.027 m, while that of the double-fault model is 0.016 m. The mean residuals are close to the observation errors (Table 1). However, the results of the two models differ significantly. The data-model correlation of the single-fault model is approximately 68.8%, which is much lower than value

of 91.4% for the double-fault model. The maximum residual of the single-fault model is 0.065 m, and the residual distribution is concentrated on the west side of the fault (Fig. 5f), indicating that observation signals cannot be simulated by the model. In addition, the single-fault model implies that most important slips occur below 18 km, which is not compatible with the aftershock relocations (Additional file 1: Figure S2). In contrast, most of the observations in the double-fault model simulation can be reconstructed, and the maximum residual is 0.043 m (Figs. 2b–d, 5e). The result from the double-fault model indicates that the rupture is mainly located at depths of 5–15 km, which fits well with the distribution of aftershocks (Fig. 3c). In general, compared with the single-fault model, the double-fault model can better explain the InSAR coseismic deformation (Figs. 2b–d, Fig. 5) and aftershock distribution of the Mainling earthquake.

Earthquake interaction and seismic risk

Model and methods

In this study, we analyze the correlation between the Mainling earthquake and historical $M_w > 7$ earthquakes on the basis of the change in Coulomb failure stress. When an earthquake occurs, seismogenic faults generate large static coseismic deformations and cause static coseismic stress changes in the near and far fields. Because of the viscoelastic lower crust and upper mantle, the seismic stress gradually relaxes and releases over time, causing ground displacement and resulting in post-seismic viscoelastic relaxation stress changes. Both coseismic and post-seismic stress adjustments can cause Coulomb stress changes in surrounding faults. According to the Coulomb failure criterion, the Coulomb stress change is defined as follows:

$$\Delta\sigma_f = \Delta\tau + \mu' \Delta\sigma_n \quad (1)$$

In the formula, $\Delta\tau$ represents the change in shear stress on the fault (positive along the slip direction of the fault); $\Delta\sigma_n$ is the change in normal stress (positive when the fault is unlocked); and μ' stands for the effective friction coefficient (ranges from 0 to 1) (Scholz 1990). In general, if historical earthquakes cause stress loading on the surrounding faults, this loading is considered to promote subsequent earthquake rupture; if historical earthquakes cause stress shadows on surrounding faults, the stress shadows postpone the occurrence of subsequent earthquakes (Stein et al. 1997).

We use the PSCMP/PSGRN software (Wang et al. 2006) to calculate the coseismic and post-seismic Coulomb stress changes on the seismogenic faults of the 2017 Mainling earthquake caused by historical $M_w > 7$ earthquakes. The PSCMP/PSGRN software is based

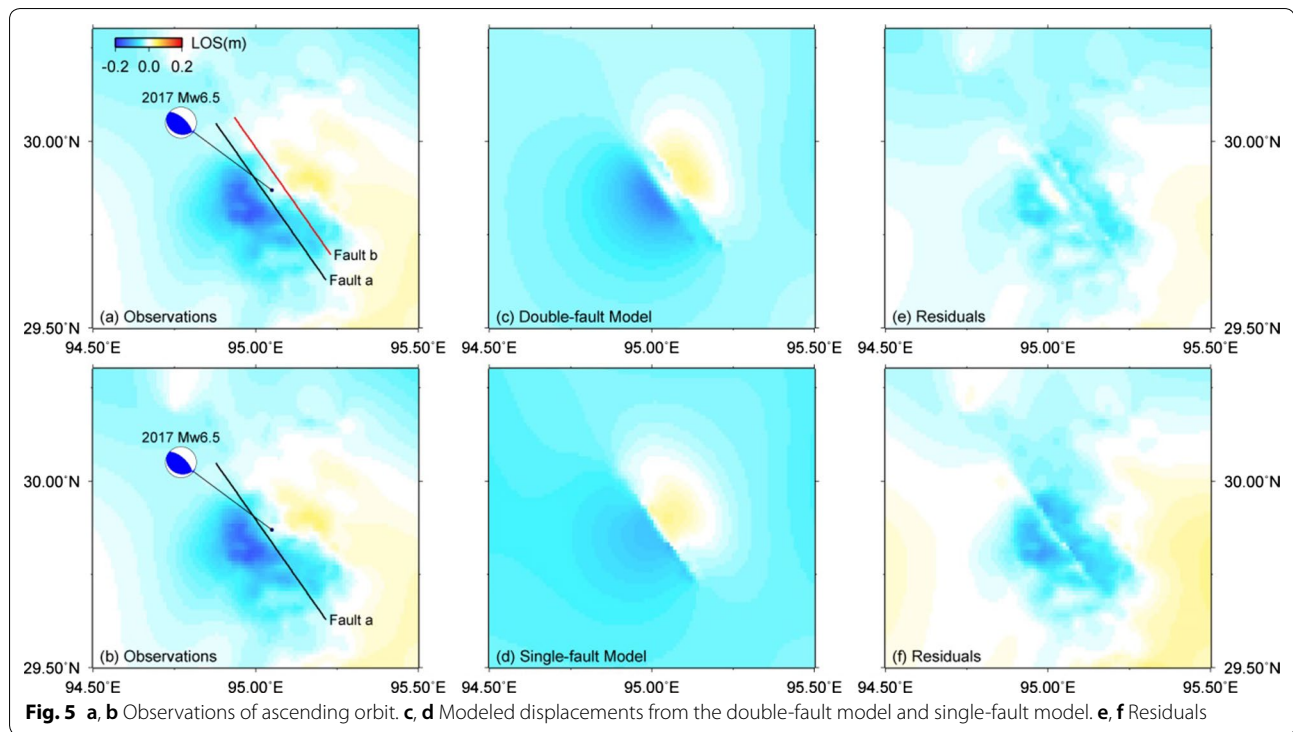
Table 2 The source parameters of the 2017 Mainling earthquake from different agencies

Source	South-dipping			North-dipping			Depth (km)	Magnitude	Location	
	Strike (°)	Dip (°)	Rake (°)	Strike (°)	Dip (°)	Rake (°)			Latitude (°)	Longitude (°)
USGS	132	55	95	303	36	83	11.5	M_w 6.4	29.829°N 94.983°E	
GCMT	109	29	56	328	66	108	12	M_w 6.5	29.70°N 95.14°E	
CENC	130	27	90	310	63	90	10	M_s 6.9	29.75°N 95.02°E	
Bai et al. (2017)	–	–	–	328	66	108	10	M_w 6.4	29.872°N 95.024°E	
Yu et al. (2018)	132.8	59	115	–	–	–	9	M_w 6.4	29.85°N 95.01°E	
Li et al. (2018)	109	29	56	–	–	–	10.5	M_w 6.5	29.8347°N 94.9002°E	
Wei et al. (2018)	–	–	–	319.9	61.7	101	12	M_w 6.45	29.87°N 95.05°E	
This paper ^s	–	–	–	328	65	94 [89.33, 109.25] ^c		M_w 6.48	29.87°N 95.04°E	
This paper ^d	Fault a	–	–	–	328	63	104 [93.58, 116.06] ^c			29.89°N 95.03°E
	Fault b	–	–	–	328	72	97 [90.11, 113.51] ^c		M_w 6.48	29.88°N 95.09°E

s: the single-fault model

d: the double-fault model

c: the mean value (lower bound, upper bound) of the rake angle

**Table 3** Stratified model composed of elastic upper crust, viscoelastic lower crust and viscoelastic mantle

Stratum	Depth (km)	P-wave velocity (km/s)	S-wave velocity (km/s)	Density (kg/m ³)	Viscosity coefficient (Pa.s)
Crust					
Upper crust	0–31.15	6.00	3.52	2720	∞
Lower crust	31.15–46.10	6.30	3.68	2790	Model 1: $\eta = 1 \times 10^{19}$ Model 2: $\eta = 5 \times 10^{19}$ Model 3: $\eta = 1 \times 10^{20}$
	46.10–62.29	6.60	3.82	2850	
Upper mantle	62.29–150	8.25	4.57	3390	1×10^{20}

This study uses a relatively simple Maxwell body model to simulate the viscoelastic lower crust and upper mantle to reduce the uncertainty from more parameters in a more complicated model (Shan et al. 2013). The stratified parameters come from the crust 1.0. In the main calculation, the viscosity coefficients of the lower crust and upper mantle are set at 1×10^{19} Pa s and 1×10^{20} Pa s, respectively (model 1; Shan et al. 2013); the viscosity coefficients of the lower crust selected by model 2 and model 3 (Yin et al. 2018a) are used in stability analysis

on the layered viscoelastic half-space crust model (Table 3), which considers gravity and can effectively simulate the coseismic and post-seismic deformation and stress changes caused by earthquakes. In this study, the apparent coefficient of friction μ' is set to a moderate value of 0.4 (King et al. 1994). Different values of μ' are tested to verify the stability of the results. Coulomb stress values are calculated at a depth of 10 km, considering the varying strike orientations of faults.

Historical earthquakes

Li et al. (2014) collected the global observational phase recordings of the M_w 7.5 Lang earthquake in 1947 and redetermined the source parameters of the earthquake using the location method provided by the China Earthquake Networks Center (CENC). On this basis, the focal mechanism solution was recalculated as strike = 195°, dip = 84°, and rake = 172°, which is consistent with the slip mechanism of the Lilong fault (Table 4).

Table 4 Hypocenter parameters of the historical earthquakes

Time	Magnitude	Epicenter location		Focal mechanism			Focal depth (km)	Slip distribution			References
		Longitude (°E)	Latitude (°N)	Strike (°)	Dip (°)	Rake (°)		Length (km)	Width (km)	Slip (m)	
1947	M_w 7.5	93.65	28.61	195	84	172	19	120.2	18.4	2.7	Li et al. (2014)
1950	M_w 8.4	96.76	28.38	303.2	63.92	164.15	11	250	80	35	Ben-Menahem et al. (1974) and Li et al. (2015)

For the 1950 Zayu earthquake, obtaining accurate fault plane solutions is difficult due to limited monitoring techniques and conditions at that time. Ben-Menahem et al. (1974) inverted its focal mechanism based on the teleseismic data recorded by global seismic stations. According to the parameters of strike = 335°, dip = 58° and rake = 176°, this earthquake was considered a right-lateral strike-slip event. Using the P-wave data collected from 239 stations worldwide and the positioning methods provided by CENC Li et al. (2015) relocated the 16 $M > 6$ events in the sequence of the Zayu earthquake. These authors argued that the focal mechanism of the main shock was strike 303.2°, dip 63.92°, rake 164.15°, which is close to the result of Ben-Menahem et al. (1974).

We selected the above two $M > 7.0$ earthquakes in the study area with clear focal mechanisms and then built homogeneous dislocation models. The rupture parameters of the 1950 Zayu earthquake are from Ben-Menahem et al. (1974), while the rupture parameters (rupture length, rupture width, slip) of the 1947 Lang earthquake are calculated based on Wells and Coppersmith's empirical equation (1994). Similar methods are widely used in studies of the stress evolution along active faults (Papadimitriou et al. 2004; Shan et al. 2013; Xiong et al. 2017).

Results

Influence of the historical earthquakes on the Mainling earthquake

We calculate the coseismic and post-seismic Coulomb stress change at the epicenter of the Mainling earthquake to assess the interactions among the historical earthquakes. The receiver fault parameters are strike = 328°, dip = 63°, rake = 105° (the slip mechanism of fault a). Figure 6 shows the combined (co- and post-seismic) Coulomb stress change caused by two strong earthquakes at the hypocenter of the Mainling earthquake. The results show that the 2017 Mainling earthquake occurred in the positive stress zone of the preceding earthquakes. When the effective friction coefficient μ is 0.4 and the viscosity coefficient of the lower crust η is 1×10^{19} Pa s, the Coulomb stress change at the hypocenter of the Mainling earthquake is 0.280 MPa. When different friction coefficients and viscosity values are selected, the main characteristics of stress evolution do not change (Fig. 6). The results of various models show that the Coulomb stress change exceeds 0.217 MPa, which is much higher than 0.01 MPa, a proposed threshold value suggested for earthquake triggering (King et al. 1994; Heidbach and Ben-Avraham 2007).

The strain rates of the main active fault zones in the Qinghai–Tibet Plateau range from 1.0×10^{-8} to

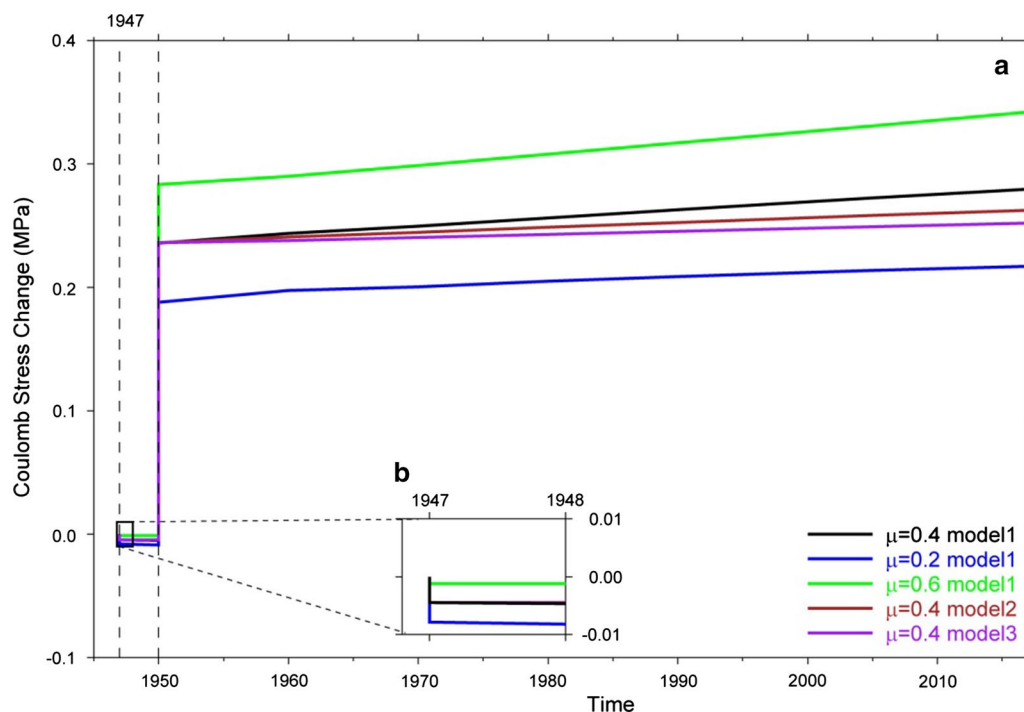


Fig. 6 **a** Coulomb stress evolution at the epicenter of the 2017 Mainling earthquake caused by historical earthquakes. Lines labeled in different colors represent results calculated with different parameters. Model 1, model 2 and model 3 indicate different viscosity coefficients, which are listed in Table 3. **b** Enlarged drawing for the period of 1947–1948

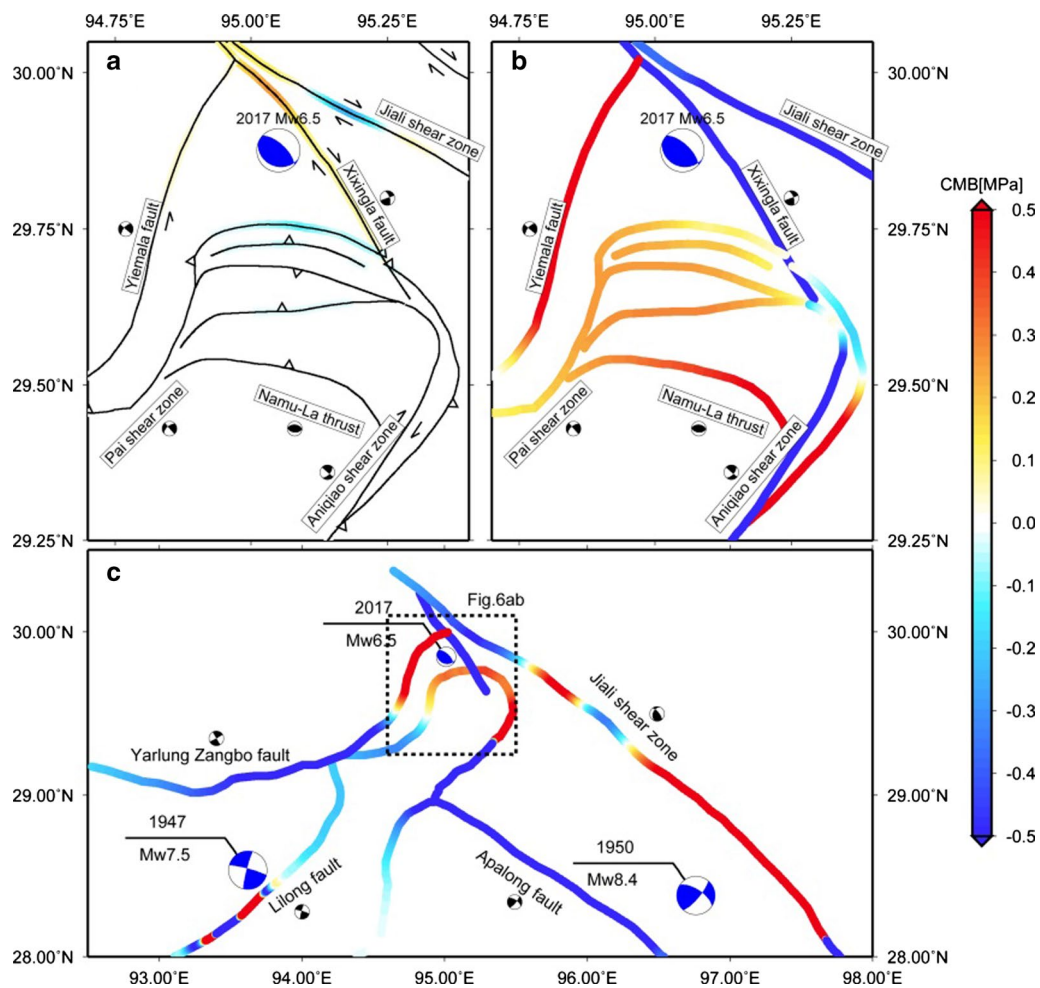


Fig. 7 **a** Coulomb stress change on surrounding faults caused by the 2017 Mainling earthquake; **b**, **c** combined Coulomb stress changes on surrounding faults in different areas caused by the 1947 Lang earthquake, the 1950 Zayu earthquake and the 2017 Mainling earthquake. The dotted line box indicates the extent of Fig. 7a, b. The blue focal spheres represent the focal mechanisms of the historical earthquakes. The black focal spheres near the fault names represent the slip mechanisms of the faults, and the parameters (Additional file 1: Table S1) are selected from Ding et al. (2001) and Yin et al. (2018a)

$4.0 \times 10^{-8}/a$ (Sun et al. 2017). When the shear modulus is 32.3 GPa and Poisson's ratio is 0.25, the calculated stress accumulation rate is approximately 1–4 kPa/a (Yin et al. 2018a). Based on this calculation, the stress change generated by the two $M > 7.0$ strong earthquakes at the hypocenter of the Mainling earthquake is equivalent to the tectonic stress accumulation over 70–280 years.

Influence of the historical earthquakes on seismic hazards of surrounding faults

Usually, a large earthquake can perturb the regional stress field and may enhance the seismic hazard in neighboring regions and faults (King et al. 1994; Shan et al. 2013). In this study, we calculate the Coulomb stress change just after 2017 event on surrounding faults caused

by the 1947 Lang earthquake, the 1950 Zayu earthquake and the 2017 Mainling earthquake (Fig. 7). In the calculation, the effective friction coefficient μ and the viscosity coefficient of the lower crust η are set at 0.4 and 1×10^{19} , respectively.

As shown in Fig. 7a, the range and magnitude of stress disturbances caused by the Mainling earthquake are relatively small, with a maximum value of 0.22 MPa on the Xixingla fault. The stress changes caused by the Mainling earthquake on other faults are not significant because the values are in the range of 10–50 kPa.

According to the stress changes produced by the three historical earthquakes (Fig. 7b, c), the 1947 Lang earthquake and the 1950 Zayu earthquake played a dominant role in the stress evolution process on the adjacent

faults. Despite the Mainling earthquake causing stress loading on the Xixingla fault, the stress unloading caused by the previous two strong earthquakes left the Xixingla fault in the stress shadow. In addition, the western section of the Jiali fault, the Apalong fault and the Aniqiao fault are in the stress shadow, and the seismic risk on these fault zones is reduced.

On the other hand, the stresses of the Namula thrust, the Yemala fault and the eastern Jiali fault are increased, with a maximum value of 2.85 MPa on the eastern Jiali fault, which is equivalent to the stress drop from a medium-sized earthquake (Zielke and Arrowsmith 2008). Both geological and geodetic data show that the slip rate along the eastern Jiali fault zone is approximately 4 mm/a (Ren et al. 2000; Lee et al. 2003; Tang et al. 2010). According to the method of Shen et al. (2003) (assuming that tectonic deformation occurs within a range of 100 km), the strike-slip rate of 4 mm/a along the eastern Jiali fault can be inferred to cause a stress accumulation rate of 1.6 kPa/a. The stress loading of 2.85 MPa is equal to the accumulation of stress over more than 1700 years.

Discussion

East-dipping model versus West-dipping model

Based on InSAR data, Yu et al. (2018) and Li et al. (2018) provided west-dipping models of the Mainling earthquake. The most significant difference between our model and the models of Yu et al. (2018) and Li et al. (2018) is that we used east-dipping plane in our model, which mainly resulted that there was a relatively big difference between our slip distribution and that of the models of Yu et al. (2018) and Li et al. (2018). We believe that compared to the west-dipping fault plane, the east-dipping fault plane is more likely to be the nodal plane of the Mainling earthquake for the following reasons:

- In the results of both Yu and Li, the relocation result of the aftershocks of the Mainling earthquake was not taken into account. The results of the aftershock (Yin et al. 2018a; Wei et al. 2018) show that the deep structure of the seismogenic fault of the Mainling earthquake should be east-dipping instead of west-dipping.
- We can well fit the InSAR observations based on the double-fault model with the east-dipping plane, and the predicted LOS displacements of double-fault model for the ascending and descending orbits are close to the results of Yu et al. 2018 and Li et al. 2018 (Additional file 1: Figure S3).
- Through the improved particle swarm optimization (Feng et al. 2013), the optimal seismogenic

fault parameters can be obtained based on nonlinear inversion of geodetic observation data, which is widely used in many earthquake cases. However, this method has its limitations: (1) This method is weak to find the optimal dip angle, so it is often necessary to perform grid search during inversion for fault slip distribution to further optimize the dip angle (e.g., Hong et al. 2018). (2) Those earthquake cases using this method have one common aspect, that is, the InSAR coseismic deformation fields resulted from these earthquakes have simple characteristics, which can be well fitted with a single-fault plane. However, in view of the complex aftershock distribution characteristics of the Mainling earthquake and the characteristics of the InSAR coseismic deformation field, it is more likely that the earthquake is a complex event. The improved particle swarm optimization may provide results that are inconsistent with the actual situation in complex events.

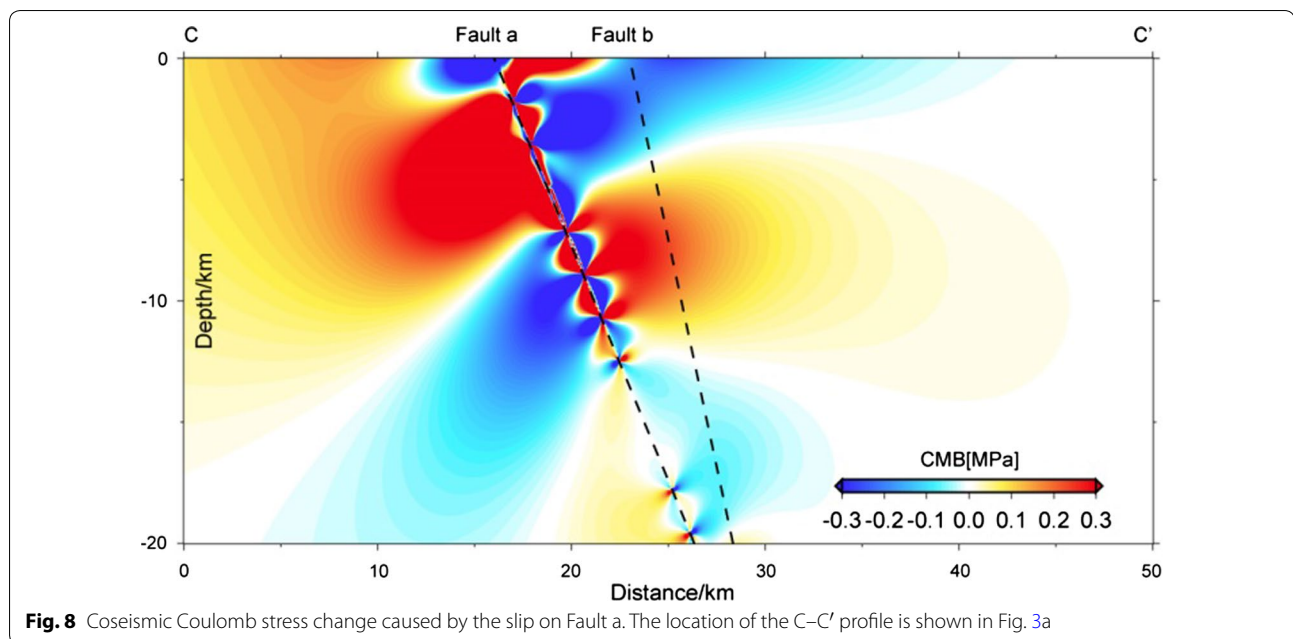
Combined rupture on two faults

Our inversion shows that the single-fault model fails to adequately interpret the observed InSAR displacement field and leaves significant residuals in the area on the west side of the fault. Moreover, the single-fault model implies that most important slips occurred below 18 km, which does not fit with the aftershock distribution. Thus, an additional segment is required to satisfactorily interpret the InSAR data and the distribution of aftershocks.

In the results provided by the double-fault model, the slips on the two faults are equivalent to moment magnitudes of M_w 6.12 (Fault a) and M_w 6.34 (Fault b), with maximum dislocation magnitudes of 0.36 m and 0.43 m, respectively. The aftershock relocation results show that rupture occurred on Fault a first and then on Fault b, accompanied by more aftershocks (Yin et al. 2018a). The spatiotemporal distribution of aftershocks is well fit with the inversion results of the double-fault model.

The case of two faults ruptured by a $M_w \approx 6.5$ earthquake is not unique, and it mostly occurs in areas with complicated tectonic settings. In 2017, the Jiuzhaigou M_w 6.5 earthquake occurred at the intersection of the East Kunlun, Tazang, Huya and Minjiang faults, with ruptures on the northern part of the Huya fault and the Minjiang fault (Sun et al. 2018). In 2018, at least three faults were involved in the M_w 6.4 Hualien earthquake in east Taiwan (Yang et al. 2018b; Huang and Huang 2018).

Our results and the aftershocks distribution indicate that Fault a may not be parallel to Fault b in the dip orientation (Fig. 3). If this phenomenon truly exists, the slip



occurring on Fault a would release the normal stress in the shallow seismogenic region of Fault b and promote the occurrence of slip on the latter. The results of the coseismic Coulomb stress change indicate that the slip on Fault a loaded the stress state on Fault b (Fig. 8), which may be one of the reasons for the rupture on two faults caused by the Mainling earthquake.

High dip angle

Our inversion results and the aftershock distribution show that the dip angle of the Mainling earthquake is 63° – 72° , which is higher than most other reverse events. For thrust earthquakes on steep faults that require strong driving force, the occurrence of a thrust event with such a high dip angle is almost impossible. However, the strong and continuous collision of the Indian Plate in the eastern syntaxis region provides the tectonic environment for a high-angle thrust earthquake.

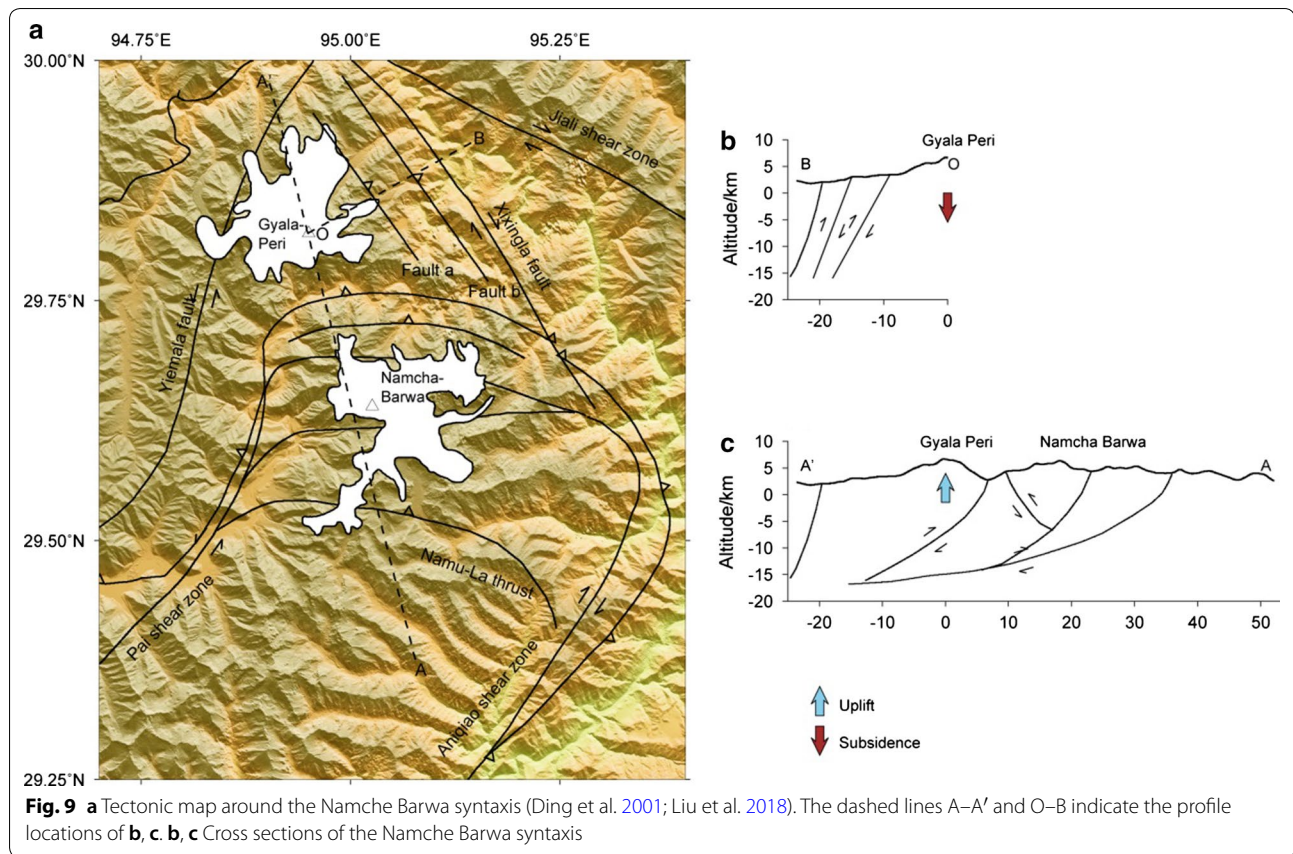
The Mainling earthquake is not the only thrust earthquake with a high dip angle. The Assam M_w 8.1 earthquake, which occurred on the Shillong Plateau in 1897, had a dip angle of 57° and caused a coseismic slip of 18 ± 7 m (Bilham 2001). Schmidt and Bürgmann (2006) inverted the focal mechanism of the 2001 Bhuj M_w 7.5 earthquake in western India with InSAR data and determined that the dip angle was 51° . He et al. (2018) considered the 2016 Nura M_w 6.5 earthquake to have occurred on a steep north-dipping fault with a dip angle of 67° based on Sentinel-1A radar interferometry constraints. The 2018 M_w 6.6 Hokkaido Eastern Iburi earthquake was

a thrust-type earthquake that occurred in the Hokkaido region of Japan, and its dip angle was 74° (Kobayashi et al. 2019). These thrust earthquakes with high dip angles all occurred in areas with strong tectonic movements.

An atypical event?

Geological data show a series of small-sized thrust faults with dip angles $>60^{\circ}$ near the Yemala fault and the Xixingla fault (Ding et al. 2001; Xu et al. 2008; Liu et al. 2018). These faults regulate a part of the dip-slip component of the subduction of the Namche Barwa syntaxis, while some of the strike-slip components are adjusted by strike-slip faults (e.g., the Yemala fault and the Xixingla fault). Such a phenomenon of “specialization and cooperation” between different types of faults widely exists in active fault systems (Wang et al. 2017).

Only 20 km from Mount Namche Barwa, Mount Gyala Peri is a geological sign of the eastern Himalayan syntaxis. The coseismic displacement field shows that the Mainling earthquake produced subsidence near Mount Gyala Peri (Fig. 2), which is obviously contrary to the uplift of Gyala Peri. As shown in Fig. 9b, c, the thrust movement on the seismogenic fault of the Mainling earthquake causes subsidence in the area near Mount Gyala Peri, while the tectonic movement of the Namula fault causes uplift. Mount Gyala Peri can possibly continue rising when the uplift movement is greater. This phenomenon indicates that the small-scale thrust faults lying near strike-slip faults and represented by the seismogenic faults of the Mainling earthquake do not play a significant role in the tectonic movement of the Namche



Barwa syntaxis. The imbricate faults represented by the Namula fault play a dominant role in the uplift process of Mount Gyala Peri (Fig. 9).

Seismic hazard assessment

The small-scale seismogenic faults of the Mainling earthquake are not typical structures in the Namche Barwa syntaxis. A series of thrust faults with larger scale and more significant movement should have the ability to generate larger earthquakes. However, the earthquake catalog shows that the seismicity on these faults is not very active, and no $M_w > 6.0$ earthquake has occurred since 1950 (Fig. 1b), which is clearly contrary to the strong tectonic setting in the Namche Barwa syntaxis. One possible explanation is that the average elevation of the Namche Barwa syntaxis is more than 3000 m, and there are two mountains with elevations of more than 7000 m. Large mountain ranges produce significant normal stresses on faults and inhibit ruptures (Styron and Hetland 2015; Yue et al. 2017; Tan et al. 2018). However, the occurrence of earthquakes could only be postponed by the normal stress from topography, not be prevented. The longer the earthquake interval is, the higher the tectonic stress accumulation, and the greater the earthquake

that may occur in the future. Historical strong earthquakes caused stress loading on these thrust faults, which increased the seismic hazard in these areas. It is possible that earthquakes larger than the $M_w 6.5$ Mainling earthquake ($M_w > 6.5$) occur on these thrust faults in the future.

Conclusions

We obtain a slip model of the 2017 Mainling earthquake utilizing InSAR data and aftershock distribution. In addition, we use the Coulomb rupture model to analyze the correlation between the Mainling earthquake and historical strong earthquake events, as well as the stress changes on the main active faults in the Namche Barwa syntaxis caused by historical strong earthquakes. Our results indicate the following:

1. The 2017 Mainling earthquake was a north-dipping event that ruptured two reverse faults on the western side of the Xixingla fault. The dip angles of the faults are 63° – 72° . The slips on the two faults are equivalent to moment magnitudes of $M_w 6.12$ and $M_w 6.34$, with maximum dislocation magnitudes of 0.34 m and 0.35 m, respectively. The complicated rupture with

high dip angles reveals strong tectonic movement beneath the Namche Barwa syntaxis.

2. The small-scale thrust faults lying near the Xixingla fault and Yemala fault, represented by the seismogenic faults of the Mainling earthquake, are not typical structures in the Namche Barwa syntaxis. Instead, the thrust movements of imbricate faults (e.g., the Namula fault) and strike-slip motions of shear zones (e.g., the Xixingla fault and the Yemala fault) are more typical tectonic movement modes in the eastern Himalayan syntaxis.
3. The coseismic and post-seismic Coulomb stress induced by the 1947 Lang earthquake and the 1950 Zayu earthquake caused stress loading at the hypocenter of the Mainling earthquake. The amount of stress change was equivalent to the tectonic stress accumulation in 70–280 years. The historical strong earthquakes caused stress unloading on the Xixingla fault, western Jiali fault, Apalong fault and Aniqiao fault, which reduced the seismic hazard in these areas. The stresses of the Yemala, Namula and eastern Jiali faults were loaded. Based on the Coulomb stress results and geological data, we believe that $M_w > 6.5$ earthquakes may occur in the Namche Barwa syntaxis and that the occurrence of historical events enhanced the seismic risk in this region.

Additional file

Additional file 1. Table S1. Receiver fault parameters for Coulomb stress change calculation in Figure 7. **Figure S1.** (a,c) Observations of descending and ascending data. (b,d) The down-sampling results of descending and ascending data. **Figure S2.** (a) Slip distribution of the single-fault model (vertical view). The solid lines A-A' indicate the seismogenic fault. (b) Slip distribution of the double-faults model (cross-sectional view). The gray star indicates the location of the hypocenter of the main shock. **Figure S3.** Double-fault model predicted LOS displacements for (a) descending orbit and (b) ascending orbit.

Abbreviations

GCMT: Global Centroid Moment Tensor; InSAR: interferometric synthetic aperture radar; ESA: European Space Agency; DEM: digital elevation model; SRTM: Shuttle Radar Topography Mission; SNAPHU: the statistical-cost network-flow algorithm for phase unwrapping; LOS: line of sight; CENC: The China Earthquake Networks Center; CMB: Coulomb stress change; CMONOC: Crustal Movement Observation Network of China.

Acknowledgements

My gratitude goes to Dr. Bin Shan at Institute of Geophysics and Geomatics, China University of Geosciences, who provided useful guidance on the operation of PSGRN/PSCMP software. Some figures were completed with Generic Mapping Tools (GMT) (Wessel and Smith 1995).

Authors' contributions

WX contributed to conceptualization; WC and XQ contributed to data curation; WC contributed to formal analysis; WX, ZN and CX contributed to funding acquisition; YW, GL and CX contributed to methodology; ZN contributed to

project administration; WX wrote the original draft; WX wrote, reviewed and edited the manuscript. All authors read and approved the final manuscript.

Authors' information

Wei Xiong is Ph.D candidate and research assistant of the Institute of Seismology, China Earthquake Administration. His research focuses on geodesy and geodynamics. He works on the coseismic, post-seismic and interseismic deformation and stress accumulation on active faults in China mainland by using GPS and InSAR.

Funding

This research was funded by the Spark Program of Earthquake Technology of CEA (XH17023Y) and the National Natural Science Foundation of China (41604079, 41504011, 41431069, 41731071).

Availability of data and materials

The datasets used during the current study are available from the corresponding author on a reasonable request.

Ethics approval and consent to participate

Not applicable.

Consent for publication

Not applicable.

Competing interests

The authors declare that they have no competing interests.

Author details

¹ Key Laboratory of Earthquake Geodesy, Institute of Seismology, CEA, Wuhan 430071, China. ² School of Geodesy and Geomatics, Wuhan University, Wuhan 430079, China.

Received: 5 March 2019 Accepted: 11 June 2019

Published online: 24 June 2019

References

- Bai L, Li G, Song B (2017) The source parameters of the M6.9 Mainling, Tibet earthquake and its tectonic implications. *Chinese Journal of Geophysics*, 60(12), 4956–4963
- Ben-Menahem A, Aboodi E, Schild R (1974) The source of the great Assam earthquake: an interplate wedge motion. *Phys Earth Planet Inter* 9(4):265–289
- Bilham R (2001) England, P. Plateau 'pop-up' in the great 1897 Assam earthquake. *Nature* 410(6830):806–809
- Burg JP, Nievorgelt P, Oberli F, Seward D, Davy P, Maurin J, Diao Z, Meier M (1998) The Namche Barwa syntaxis: evidence for exhumation related to compressional crustal folding. *J Asian Earth Sci* 16(2–3):239–252
- Chen C, Zebker HA (2000) Network approaches to two dimensional phase unwrapping: intractability and two new algorithms. *J Opt Soc Am A Opt Image Sci Vis* 17(3):401
- Ding L, Zhong D, Yin A, Kapp P, Harrison TM (2001) Cenozoic structural and metamorphic evolution of the eastern Himalayan syntaxis (Namche Barwa). *Earth Planet Sci Lett* 192(3):423–438
- Ding L, Kapp P, Wan X (2005) Paleocene-Eocene record of ophiolite obduction and initial India-Asia collision, south central Tibet. *Tectonics* 24(3):1–18
- Feng W, Li Z, Elliott JR, Fukushima Y, Hoey T, Singleton A, Cook R, Xu Z (2013) The 2011 MW 6.8 Burma earthquake: Fault constraints provided by multiple SAR techniques. *Geophys J Int* 195:650–660
- He P, Hetland EA, Niemi NA, Wang Q, Wen Y, Ding K (2018) The 2016 M_w 6.5 Nura earthquake in the Trans Alai range, northern Pamir: possible rupture on a back-thrust fault constrained by Sentinel-1A radar interferometry. *Tectonophysics*. <https://doi.org/10.1016/j.tecto.2018.10.025>
- Heidbach O, Ben-Avraham A (2007) Stress evolution and seismic hazard of the Dead Sea fault system. *Earth Planet Sci Lett* 257:299–312
- Hong S, Zhou X, Zhang K, Meng G, Dong Y, Su X, Zhang L, Li S, Ding K (2018) Source model and stress disturbance of the 2017 Jiuzhaigou M_w 6.5 earthquake constrained by InSAR and GPS measurements. *Remote Sens* 10(9):1400. <https://doi.org/10.3390/rs10091400>

- Hu S, Yao H (2018) Crustal velocity structure around the eastern Himalayan syntaxis: implications for the nucleation mechanism of the 2017 M_s 6.9 Mainling earthquake and regional tectonics. *Tectonophysics* 744:1–9
- Huang M, Huang H (2018) The complexity of the 2018 M_w 6.4 Hualien earthquake in east Taiwan. *Geophys Res Lett*. <https://doi.org/10.1029/2018gl108082>
- Jonsson S, Zebker H, Segall P, Amelung F (2002) Fault slip distribution of the 1999 M_w 7.1 Hector Mine, California, earthquake, estimated from satellite radar and GPS measurements. *Bull Seismol Soc Am* 92:1377–1389
- King GCP, Stein RS, Lin J (1994) Static stress changes and the triggering of earthquakes. *Bull Seismol Soc Am* 84:935–953
- Kobayashi T, Kyonosuke H, Yurai H (2019) Geodetically estimated location and geometry of the fault plane involved in the 2018 Hokkaido Eastern Iburi earthquake. *Earth Planets Space* 71:62. <https://doi.org/10.1186/s40623-019-1042-6>
- Lee H, Chung S, Wang J, Wen D, Lo C, Yang T, Zhang Y, Xie Y, Lee T, Wu G, Ji J (2003) Miocene Jiali faulting and its implications for Tibetan tectonic evolution. *Earth Planet Sci Lett* 205(3–4):185–194
- Li B, Diao G, Zou L, Xu X, Feng X (2014) The redetermination of the source parameters of the big earthquake $M7.7$ in the southeast of Lang country in Tibet in 1947. *Seismol Geomagn Obs Res* 1:85–91
- Li B, Diao G, Xu X, Wan Y, Feng X, Zou L, Miao C (2015) Redetermination of the source parameters of the Zayü, Tibet $M8.6$ earthquake sequence in 1950. *Chin J Geophys* 58(11):4254–4265
- Li W, Xu C, Yi L, Wen Y, Zhang X (2018) Source parameters and seismogenic structure of the 2017 M_w 6.5 Mainling earthquake in the Eastern Himalayan Syntaxis (Tibet, China). *J Asian Earth Sci*. <https://doi.org/10.1016/j.jseae.2018.07.027>
- Liu Y, Shan X, Zhang Y, Zhao D, Qu C (2018) Use of seismic waveforms and InSAR data for determination of the seismotectonics of the Mainling M_s 6.9 earthquake on Nov 18 2017. *Seismol Geol* 1:1. <https://doi.org/10.3969/j.issn.0253-4967.2018.06.005>
- Okada Y (1992) Internal deformation due to shear and tensile faults in a half-space. *Bull Seismol Soc Am* 82:1018–1040
- Papadimitriou E, Wen X, Karakostas V, Jin X (2004) Earthquake triggering along the Xianshuihe Fault zone of western Sichuan, China. *Pure appl Geophys* 161:1683–1707
- Parsons B, Wright T, Rowe P, Andrews J, Jackson J, Walker R, Engdahl ER (2006) The 1994 Sefidabeh (eastern Iran) earthquakes revisited: new evidence from satellite radar interferometry and carbonate dating about the growth of an active fold above a blind thrust fault. *Geophys J Int* 164(1):202–217
- Ren J, Shen J, Cao Z (2000) Quaternary faulting of Jiali fault, southeast Tibetan plateau. *Seismol Geol* 22(4):344–350
- Schmidt DA, Bürgmann R (2006) InSAR constraints on the source parameters of the 2001 Bhuj earthquake. *Geophys Res Lett* 33(2):L02315
- Scholz CH (1990) The mechanics of earthquakes and faulting. Cambridge Univ Press, New York, p 439
- Shan B, Xiong X, Wang R, Zheng Y, Yang S (2013) Coulomb stress evolution along Xianshuihe-Xiaojiang Fault System since 1713 and its interaction with Wenchuan earthquake, May 12, 2008. *Earth Planet Sci Lett* 377:199–210
- Shen Z, Wan Y, Gan W (2003) Viscoelastic triggering among large earthquakes along the eastern Kunlun fault system. *Chin J Geophys* 46(6):786–795
- Simons M, Fialko Y, Rivera L (2002) Coseismic deformation from the 1999 M_w 7.1 Hector Mine, California, Earthquake as inferred from InSAR and GPS observations. *Bull Seismol Soc Am* 92(4):1390–1402
- Stein RS, Barka AA, Dieterich JH (1997) Progressive failure on the North Anatolian fault since 1939 by earthquake stress triggering. *Geophys J Int* 128:594–604
- Styron RH, Hetland EA (2015) The weight of the mountains: constraints on tectonic stress, friction, and fluid pressure in the 2008 Wenchuan earthquake from estimates of topographic loading. *J Geophys Res Solid Earth* 120:2697–2716
- Sun Y, Guo C, Wu Z, Fan T, Li H (2017) Numerical study of the crustal stress, strain rate and fault activity in the Eastern Tibetan plateau. *Acta Geosci Sin* 38(3):385–392
- Sun J, Yue H, Shen Z, Fang L, Zhan Y, Sun X (2018) The 2017 Jiuzhaigou earthquake: a complicated event occurred in a young fault system. *Geophys Res Lett* 45(5):2230–2240
- Tan X, Yue H, Liu Y, Xu X, Shi F, Xu C, Ren Z, Shyu J, Lu R, Hao H (2018) Topographic loads modified by fluvial incision impact fault activity in the Longmenshan thrust belt, eastern margin of the Tibetan Plateau. *Tectonics* 37:3001–3017
- Tang F, Song J, Cao Z, Deng Z, Wang M, Xiao G, Chen W (2010) The movement characters of main faults around Eastern Himalayan Syntaxis revealed by the latest GPS data. *Chin J Geophys* 53(9):2119–2128
- Tapponnier P, Xu Z, Roger F, Meyer B, Arnaud N, Wittlinger G, Yang J (2001) Oblique stepwise rise and growth of the Tibet plateau. *Science* 294:1671–1677
- Wang R (2010) The dislocation theory: a consistent way for including the gravity effect in (visco)elastic plane-earth models. *Geophys J R Astron Soc* 161(1):191–196
- Wang R, Lorenzo-Martin F, Roth F (2006) PSGRN/PSCMP—a new code for calculating co- and post-seismic deformation, geoid and gravity changes based on the viscoelastic-gravitational dislocation theory. *Comput Geosci* 32(4):527–541
- Wang H, Liuzeng J, Ng AHM, Ge L, Javede F, Long F, Aoudia A, Feng J, Shao Z (2017) Sentinel-1 observations of the 2016 Menyuan earthquake: a buried reverse event linked to the left-lateral Haiyuan fault. *Int J Appl Earth Obs Geoinf* 61:14–21
- Wei W, Xie C, Zhou B, Guo Z, Yin X, Li B, Wang P, Dong S, Wei F, Wang Y (2018) Location of mainshock and aftershock sequences of the $M6.9$ Mainling earthquake, Tibet. *Chin Sci Bull* 63(15):1493–1501
- Wells DL, Coppersmith KJ (1994) New empirical relationships among magnitude, rupture length, rupture width, rupture area, and surface displacement. *Bull Seismol Soc Am* 84:974–1002
- Wessel P, Smith WHF (1995) New version of the Generic Mapping Tools released. *EOS Trans AGU* 76:329
- Xiong W, Tan K, Qiao X, Liu G, Nie Z (2017) Coseismic, postseismic and interseismic coulomb stress evolution along the Himalayan main frontal thrust since 1803. *Pure appl Geophys* 174:1889–1905
- Xu Z, Cai Z, Zhang Z, Li H, Chen F, Tang Z (2008) Tectonics and fabric kinematics of the Namche Barwa terrane, Eastern Himalayan Syntaxis. *Acta Petrol Sin* 24(7):1463–1476
- Yang R, Herman F, Fellin MG, Maden C (2018a) Exhumation and topographic evolution of the Namche Barwa Syntaxis, eastern Himalaya. *Tectonophysics* 722:43–52
- Yang Y, Hu J, Tung H, Tsai M, Chen Q, Xu Q, Zhang Y, Zhao J, Liu G, Xiong J, Wang J, Yu B, Chiu C, Su Z (2018b) Co-seismic and Postseismic Fault Models of the 2018 M_w 6.4 Hualien earthquake occurred in the junction of collision and subduction boundaries offshore Eastern Taiwan. *Remote Sens* 10:1372. <https://doi.org/10.3390/rs10091372>
- Yin A, Harrison TM (2000) Geologic evolution of the Himalayan-Tibetan Orogen. *Earth Planet Sci* 28:211–280
- Yin X, Zhou B, Chen J, Wei W, Xie C, Guo Z (2018a) Spatial-temporal distribution characteristics of early aftershocks following the $M6.9$ Mainling earthquake in Tibet, China. *Chin J Geophys* 61(6):2322–2331
- Yin F, Jiang C, Han L, Shi Y (2018b) Seismic hazard assessment for the Red River fault: insight from Coulomb stress evolution. *Chin J Geophys* 61(1):183–198
- Yu C, Li Z, Chen J, Hu J (2018) Small magnitude co-seismic deformation of the 2017 M_w 6.4 Nyingchi earthquake revealed by InSAR measurements with atmospheric correction. *Remote Sens* 10:684. <https://doi.org/10.3390/rs10050684>
- Yue H, Ross ZE, Liang C, Michel S, Fattahi H, Fielding E, Moore A, Liu Z, Jia B (2017) The 2016 Kumamoto M_w = 7.0 earthquake: a significant event in a fault–volcano system. *J Geophys Res Solid Earth* 122:9166–9183. <https://doi.org/10.1002/2017JB014525>
- Zeitler PK, Meltzer AS, Brown L, Kidd WSF, Lim C, Enkelmann E (2014) Tectonics and topographic evolution of Namche Barwa and the easternmost Lhasa block, Tibet. *Geol Soc Am* 507:23–58
- Zielke O, Arrowsmith JR (2008) Depth variation of coseismic stress drop explains bimodal earthquake magnitude–frequency distribution. *Geophys Res Lett* 35:L24301

Publisher's Note

Springer Nature remains neutral with regard to jurisdictional claims in published maps and institutional affiliations.